Title	Characterization of Ultrathin Conductive Films Using a Simplified Approach for Terahertz Time-Domain Spectroscopic Ellipsometry
Author(s)	Nagai, Masaya; Watanabe, Sou; Imamura, Ryosuke et al.
Citation	Journal of Infrared, Millimeter, and Terahertz Waves. 2024, 45(11-12), p. 949-966
Version Type	VoR
URL	https://hdl.handle.net/11094/98278
rights	This article is licensed under a Creative Commons Attribution 4.0 International License.
Note	

RESEARCH

Characterization of Ultrathin Conductive Films Using a Simplified Approach for Terahertz Time-Domain Spectroscopic Ellipsometry

Masaya Nagai[1] (ID) **· Sou Watanabe[1] · Ryosuke Imamura[1] · Masaaki Ashida[1] · Kohei Shimoyama[2] · Haobo Li[2] · Azusa N. Hattori[2] · Hidekazu Tanaka[2]**

Abstract

We present two ideas to simplify the measurement and analysis of terahertz time-domain spectroscopic ellipsometry data of ultrathin films. The measurement is simplified by using a specially designed sample holder with mirrors, which can be mounted on a cryostat. It allows us to perform spectroscopic ellipsometry by simply inserting the holder into a conventional terahertz spectroscopy system for measurements in transmission geometry. The analysis of the obtained data is simplified by considering a single interface with a certain sheet conductivity σ_s (since the film thickness is significantly smaller than the wavelength of the terahertz light). We demonstrate the application of these ideas by evaluating the sheet conductivities of two perovskite rare-earth nickelate thin films in the temperature range 78–478 K. The use of this particular analytical method and the sample holder design will help to establish terahertz time-domain spectroscopic ellipsometry as a characterization technique for ultrathin films.

✉ Masaya Nagai
  mnagai@mp.es.osaka-u.ac.jp

[1] Graduate School of Engineering Science, Osaka University, 1-3 Machikaneyama Toyonaka, Osaka 560-8531, Japan

[2] SANKEN (Institute of Scientific and Industrial Research), Osaka University, 8-1 Mihogaoka, Ibaraki, Osaka 567-0047, Japan

◢ Springer

1 Introduction

Spectroscopic ellipsometry is a characterization technique where the optical constants of a sample are evaluated by measuring the change in the polarization that occurs when the probe light is reflected from the sample at oblique incidence. From the ellipsometry coefficient $\rho = r_p/r_s$ (the ratio of the complex reflection coefficients), we can obtain the refractive index n, the extinction coefficient κ and the surface roughness of the measured sample. Since spectroscopic ellipsometry is sensitive to extremely thin films and their interfaces, it also allows us to evaluate the layer thicknesses in a multilayer sample [1]. Spectroscopic ellipsometry is an established characterization technique in various areas of science and industry including areas concerned with semiconductors, and many ellipsometer systems with a broad wavelength coverage from the ultraviolet to the infrared are commercially available. This technique is also applicable to the terahertz (THz) frequency range [2], and many important material properties, such as dielectric properties and electric conductivity, are related to states that can be excited with THz photons [3]. THz spectroscopic ellipsometry is a powerful technique, especially for thin films on thick absorbing substrates, which are difficult to characterize by conventional transmission measurements [4]. It is powerful because spectroscopic ellipsometry is self-referencing, and thus solves the phase uncertainty problem in a reflection measurement [5, 6]. THz spectroscopic ellipsometry was first demonstrated in 2001 by Nagashima and Hangyo, based on THz time-domain spectroscopy [7], and since then, THz spectroscopic ellipsometry has been used successfully in many investigations [8–21].

Here, we present two approaches to simplify the characterization of ultrathin conductive films using THz time-domain spectroscopic ellipsometry. The first approach is to use an analysis model that treats the film as a single interface with sheet conduction, rather than assuming a complex structure of dielectric multilayers. This analysis method is commonly used to determine the optical responses of graphene [22, 23] and is applicable to layers that are sufficiently thin compared to the wavelength of the used THz light. The approach of using a conductive sheet model is applied in the well-known Tinkham's equation for normal incidence [24], which is used for the analysis of superconducting thin films with THz spectroscopy. The second approach is a specially designed sample holder in a cryostat that allows us to perform THz spectroscopic ellipsometry measurements easily. Typically, when evaluating the temperature dependence of optical constants, a cryostat with a window oriented in a specific direction is required. However, by integrating mirrors into the sample holder mounded on a cryostat, the incident and reflected light can be aligned coaxially. This allows for spectroscopic ellipsometry to be performed by simply inserting the holder into a conventional THz spectroscopy system designed for transmission geometry. The proposed design is similar to that of the Dove prism used in THz time-domain attenuated total internal reflection spectroscopy [25, 26]. Previously, we performed THz time-domain spectroscopy measurements at low temperatures using a sample holder that enables reflection measurements at an incident angle of 30° [27–29]. We redesigned

this sample holder for high-temperature measurements at an incident angle of 60°. The presented ideas are demonstrated by evaluating the sheet conductivities of two perovskite rare-earth nickelate thin films in the temperature range 78–478 K.

2 The Conductive Sheet Model

We first consider an ultrathin film with thickness d. The complex refractive index of this film is denoted by n_f, and the film is placed on a substrate (with refractive index n_2) in vacuum ($n_1 = 1$), as shown in Fig. 1a. If d is sufficiently small compared to the wavelength of the light, λ, we can consider the film as an interface between the vacuum region and the substrate with a zero-thickness sheet conductivity of $\sigma_s = -i\omega\epsilon_0(n_f^2 - n_2^2)d$, as shown in Fig. 1b. According to the boundary conditions for Maxwell's equations, the electric fields parallel to the interface is continuous, and the difference between the magnetic fields is the sheet current, which is induced by the electric field on the substrate side and the sheet conductivity σ_s. Thus, the complex reflection coefficients r_p and r_s for the angle of incidence θ_1 can be expressed as follows [23]:

$$r_p = \frac{(n_2 + Z_0\sigma_s\cos\theta_2)\cos\theta_1 - n_1\cos\theta_2}{(n_2 + Z_0\sigma_s\cos\theta_2)\cos\theta_1 + n_1\cos\theta_2},$$ (1)

$$r_s = \frac{n_1\cos\theta_1 - n_2\cos\theta_2 - Z_0\sigma_s}{n_1\cos\theta_1 + n_2\cos\theta_2 + Z_0\sigma_s}.$$ (2)

Here, $Z_0 = 377\ \Omega$ is the vacuum impedance, and θ_2 is a complex parameter satisfying $n_1\sin\theta_1 = n_2\sin\theta_2$. If we derive the complex transmission coefficients in a similar way, we can obtain Tinkham's equation for normal incidence [24]. The derivation of these equations is shown in Sections 1 and 2 of the Supplementary Information. Recently, Watanabe et al. proposed an analytical model for expanding the equivalent electrical transmission circuit to a finite angle of incidence based on a multilayer-film model [30]. Their proposed equations are the same as Eqs. (1) and (2).
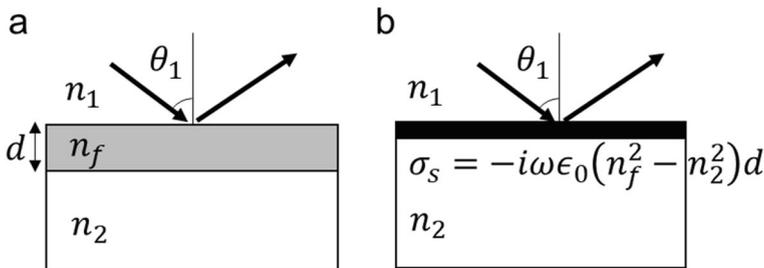

Fig. 1 **a** The considered single-layer model and (**b**) the corresponding conductive sheet model for $d \ll \lambda$

The conductive sheet model helps us intuitively understand the contribution of σ_s to r_p. Li et al. experimentally demonstrated that the dielectric constant of a thin film can be evaluated under the Brewster condition [31], which can be easily understood from Eq. (1): Under the Brewster condition for the substrate ($n_2\cos\theta_1 - n_1\cos\theta_2 = 0$), the numerator of r_p is $Z_0\sigma_s\cos\theta_1\cos\theta_2$. This suggests that r_p is more sensitive to σ_s than r_s at large incident angle, and also means that approximating σ_s with a real number changes the predicted Brewster angle depending on the contribution of σ_s. Furthermore, Eq. (1) shows that the refractive index n_2 and $Z_0\sigma_s$ contribute to the same degree, which means that spectroscopic ellipsometry is suitable for measuring sheet conductivities on the order of milliSiemens ($Z_0\sigma_s \approx 1$).

The conductive sheet model has also the advantage that σ_s can be easily derived from the ellipsometry coefficient ρ. The analytical expression for ρ is given in Eq. (3) below.

$$\rho = \frac{r_p}{r_s} = \frac{\left(n_2\cos\theta_1 - n_1\cos\theta_2\right)/\cos\theta_1\cos\theta_2 + Z_0\sigma_s}{\left(n_2\cos\theta_1 + n_1\cos\theta_2\right)/\cos\theta_1\cos\theta_2 + Z_0\sigma_s} \times \frac{\left(n_1\cos\theta_1 + n_2\cos\theta_2\right) + Z_0\sigma_s}{\left(n_1\cos\theta_1 - n_2\cos\theta_2\right) - Z_0\sigma_s}$$
(3)

This equation can be rewritten as $\rho = (A + Z_0\sigma_s)(C + Z_0\sigma_s)/(B + Z_0\sigma_s)(D - Z_0\sigma_s)$, and thus σ_s can be obtained by solving a quadratic equation (numerical calculations are not necessary).

$$\sigma_s = \frac{1}{2(\rho+1)Z_0}\left[-(A + C + \rho(B-D)) \pm \sqrt{(A + C + (B-D)\rho)^2 - 4(\rho+1)(AC - \rho BD)}\right]$$
(4)

$A = \left(n_2\cos\theta_1 - n_1\cos\theta_2\right)/\cos\theta_1\cos\theta_2$
$B = \left(n_2\cos\theta_1 + n_1\cos\theta_2\right)/\cos\theta_1\cos\theta_2$
$C = n_1\cos\theta_1 + n_2\cos\theta_2$
$D = n_1\cos\theta_1 - n_2\cos\theta_2$

There are two solutions to the above equation, but we used the positive solution in the analysis in Section 6.

3 Comparison Between the Conductive Sheet Model and the Multi-Layer Model

In order to confirm the validity of the conductive sheet model, we compare the reflection coefficients predicted by the conductive sheet model and the conventional multi-layer model, which is explained in Sections 3 and 4 of the Supplementary Information. We assume a film thickness of $d = 1$ μm and p-polarized light at an angle of incidence of 60°. The calculation results for s-polarized light are provided in Fig. S1 of the Supplementary Information.

Figure 2a shows r_p as a function of the frequency of the p-polarized light for $n_f = 5$ and $n_2 = 3.4$. Figures 2b and 2c show the results for different values of n_f. The thick solid and thick broken curves represent the amplitude and phase of r_p predicted by the conductive sheet model, respectively, and the thin solid and thin
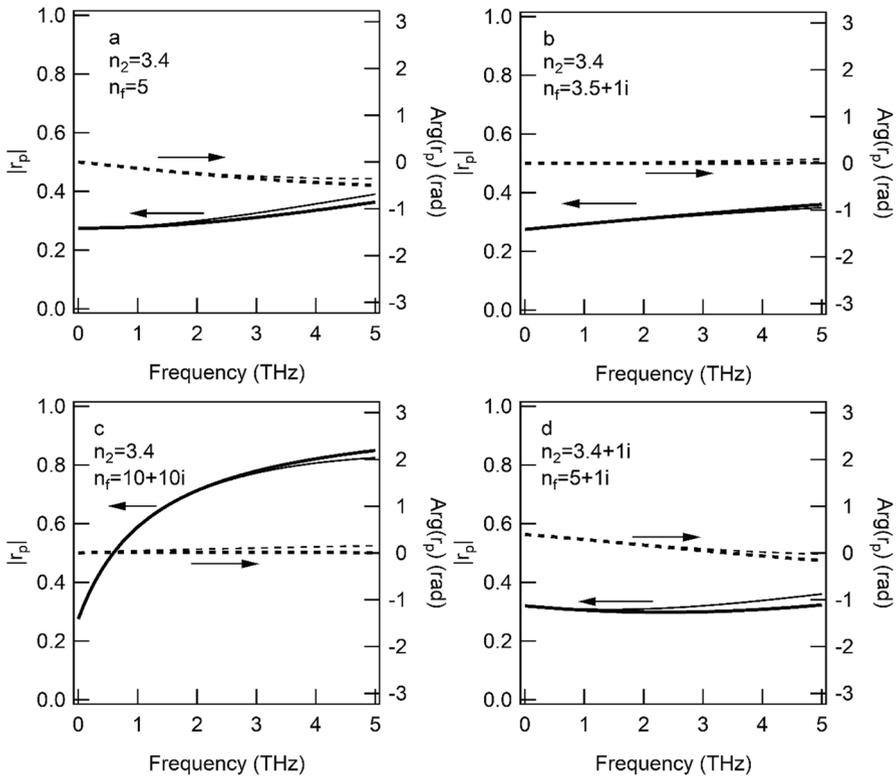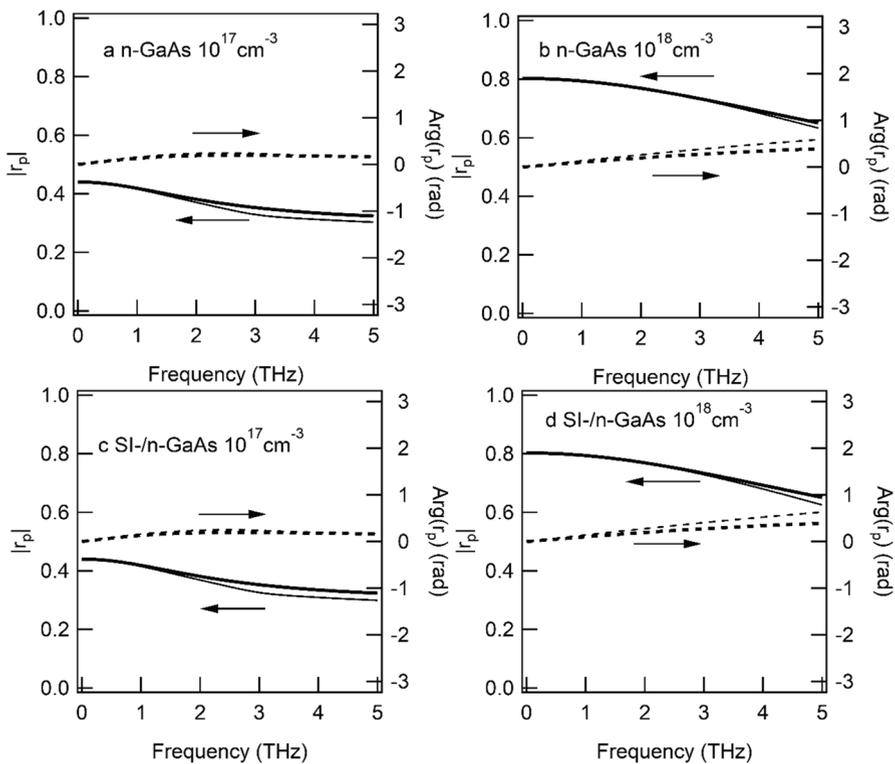
Fig. 2 Complex reflection coefficients in the case of a film thickness of $d=1$ μm and p-polarized light with an angle of incidence of 60°. (**a**) The data for a thin film with $n_f = 5$ and a substrate with $n_2 = 3.4$. (**b**), (**c**) The data for $n_f = 3.5 + 1i$ and $10 + 10i$, respectively. (**d**) The data for a thin film with $n_f = 5 + 1i$ and $n_2 = 3.4 + 1i$. The solid and broken curves represent the amplitude and phase of the complex reflection coefficient, respectively, and the thick and thin curves represent the calculation results of the conductive sheet model and the single-layer model, respectively

broken curves show the calculation results of the single-layer model. If there is no absorption in the thin film, which is the case in Fig. 2a, interference appears at high frequencies, whereas it is small at low frequencies. This behavior can be explained by the conductive sheet model: the dielectric thin film has a small contribution to the complex reflectance at low frequencies due to the surface conductivity $\sigma_s = -i\omega\chi \propto \omega$. Figure 2 suggests that the conductive sheet model is sufficiently accurate below 2 THz for film thicknesses less than 1 μm. In the case of $n_f = 3.5 + 1i$ and $n_2 = 3.4$, in which $\text{Re}[\sigma_s]$ is much larger than $\text{Im}[\sigma_s]$ from $\sigma_s = -i\omega\epsilon_0\left(n_f^2 - n_2^2\right) = (7 + 0.31i)\omega\epsilon_0$, the change in $|r_p|$ calculated for both models is also the same below 2 THz and $\text{Arg}\left(r_p\right)$ is constant, as shown in Fig. 2b. Figure 2c shows the results for stronger absorption ($\sigma_s = (200 + 11.56i)\omega\epsilon_0$). As can be seen in Figs. 2b and 2c, a thin conductive film has a significant effect on the amplitude of the complex reflection coefficient. Additionally, we find that the conductive sheet model can be used for film thicknesses less than 1μm, which is less

than 1/100 of the wavelength. We also calculated the reflection in the case of absorption in the substrate ($n_f = 5 + 1i$, $n_2 = 3.4 + 1i$) as shown in Fig. 2d. The prominent features are almost the same.

Next, we performed calculations for GaAs, which is a realistic material exhibiting dispersion. Figures 3(a) and (b) show r_p as a function of the frequency of the p-polarized light for an n-doped GaAs thin film with a thickness of 1 μm on a semi-insulating GaAs substrate, with carrier densities of 10^{17}cm^{-3} and 10^{18}cm^{-3}, respectively. The thick solid and thick dashed curves represent the amplitude and phase of r_p predicted by the conductive sheet model, respectively, while the thin solid and thin dashed curves show the results calculated using the single-layer model. The dielectric constant was taken from previously measured data [28]. The complex reflectance for s-polarized light is provided in Fig. S3 of

Fig. 3 Complex reflection coefficients in the case of a 1 μm-thick n-GaAs film on the semi-insulating GaAs substrate and p-polarized light with an angle of incidence of 60°. The refractive index of n-GaAs can be written as $n^2(\omega) = \epsilon_b - (ne^2/\epsilon_0 m_e^*)/(\omega^2 + i\omega/\tau)$, where $\epsilon_b = 12.8$, $m_e^* = 0.067m_0$, and $\tau = 92$ fs (ϵ_b is the background dielectric constant, m_0 is the mass of free electron, and τ is the scattering time). Carrier density of n-GaAs is (**a**) $n = 10^{17}$cm^{-3} and (**b**) 10^{18}cm^{-3}, and that of semi-insulating GaAs is $n = 0$ cm^{-3}. Figures (**c**) and (**d**) show complex reflection coefficients when a 0.1 μm thick semi-insulating GaAs film is layered on the thin film assumed in Figures (a) and (b), respectively. The solid and broken curves in all figures represent the amplitude and phase of the complex reflection coefficient, respectively, and the thick and thin curves represent the calculation results of the conductive sheet model and the multilayer model, respectively

the Supplementary Information. Both spectra show nearly identical results in the frequency range below 2 THz. Therefore, we conclude that the conductive sheet model is applicable to real materials with dispersion.

In the conductive sheet model, the complex reflectance is calculated by simplifying the structure to a zero-thickness conduction sheet. This approximation remains valid even when a dielectric multilayer with a total thickness much shorter than the wavelength lies on a substrate, a scenario in which the single-layer model is no longer applicable. In general, semiconductor thin films often have a cap layer on the surface. According to the conductive sheet model, we predict that this semi-insulating layer does not contribute to the reflection coefficient due to the absence of surface current. To verify this, we calculated the reflectance for a structure consisting of a semi-insulating GaAs layer with a thickness of 0.1 μm, a 1 μm thick n-GaAs layer, and a semi-insulating GaAs substrate. Figures 3(c) and 3(d) show the r_p values calculated using both the conductive sheet model and the double-layer model with different carrier concentrations in the n-GaAs layer. The spectral shapes calculated by both models are clearly identical below 2 THz.

In spectroscopic ellipsometry, the pseudo-dielectric function $\langle \epsilon \rangle$ is often used as an approximation for thin films within a dielectric multilayer model [1, 14]. This approach utilizes the change in the effective dielectric constant of the substrate in spectroscopic ellipsometry when a thin film is present on the surface. The pseudo-dielectric function $\langle \epsilon \rangle$ can be expressed as a function of the ellipsometric parameters which can be expressed by r_p and r_s in a dielectric multilayer model. Thus, the dielectric constant of the thin film can be derived by differentiating $\langle \epsilon \rangle$ with respect to the film thickness d. This expression includes terms of σ_s. In the conductive sheet model, the dielectric response in the thin film is first approximated as a surface current at the interface with no thickness, and we then discuss how this affects the complex reflectance of p-polarized and s-polarized light. If we consider a quantity analogous to the pseudo-dielectric function, we can define the pseudo-refractive index for p-polarized and s-polarized light as follows by comparing Eqs. (1) and (2) with the Fresnel coefficients:

$$\langle n_2 \rangle_p = n_2 + Z_0 \sigma_s \cos \theta_2, \langle n_2 \rangle_s = n_2 + Z_0 \sigma_s / \cos \theta_2 \tag{5}$$

This provides an intuitive and physically insightful understanding. However, the above expressions in the conductive sheet model do not exhibit the anomalies at $\epsilon_f = 0$ and $\epsilon_2 = 1$ that are apparent in pseudo-dielectric functions $\langle \epsilon \rangle$ [14]. This suggests that surface plasmons polariton or surface-guided waves cannot be described by the conductive sheet model with the assumption of no current perpendicular to the surface. This represents a condition in which the conductive sheet model is not applicable.

4 Design of a Compact Sample Holder

In order to demonstrate thin-film characterization using THz spectroscopic ellipsometry easier, we designed a sample holder with mirrors mounted on a cryostat that can be used to perform reflection measurements by inserting it in a conventional

THz spectroscopy system for measurements in transmission geometry. The design is shown in Fig. 4a. If we use the two mirror surfaces of the prism at the bottom and consider a plane wave entering the system parallel to the base of the prism, the light is incident on the sample at a certain angle θ_1 and exits the system coaxially if the sample position is correctly chosen. The angle θ_1 and the apex angle α of the prism mirror satisfy the relation $\theta_1 + 2\alpha = 90°$ (on the mirror surface, the incident angle is 90°-α). The size of the prism is determined by the beam diameter $2h$ as shown in the figure. The prism length is $W = 4h/\tan\alpha$, and the distance from the optical axis to the sample is $p = 2h/(1 - \tan^2\alpha)$. If we assume $\theta_1 = 60°$ and $2h = 6$ mm, we obtain $\alpha = 15°$, $p = 6.46$ mm, and $W = 44.8$ mm. This holder can be mounted in a cryostat.

In the experiment, we need to consider that inserting this sample holder (which extends the optical path length) changes the optimal detector focal plane. The optical path length change determined by the geometry in Fig. 4a is $\Delta L = W(1/\cos 2\alpha - 1)/2 = 3.46$ mm. This can be corrected by slightly adjusting the emitter and detector positions. Furthermore, we need to consider the uncertainty in the angle of incidence, $\Delta\theta_1$, when inserting this small sample holder at the sample focal plane of the experimental setup. As shown in Fig. 4b, the cone angle of the beam probing the sample center corresponds to a numerical aperture of $NA = 0.125$, which is determined by the size of the sample holder. By assuming a Gaussian beam and $\lambda = 0.3$ mm (corresponding to 1 THz), the beam waist radius at the focal plane is $w_0 = \lambda/\pi NA = 0.76$ mm, and the Rayleigh length is $z_R = \pi w_0^2/\lambda = 6.0$ mm. While the incident angle may shift at both ends of the irradiation spot on the sample, its uncertainty is very small ($\Delta\theta_1$
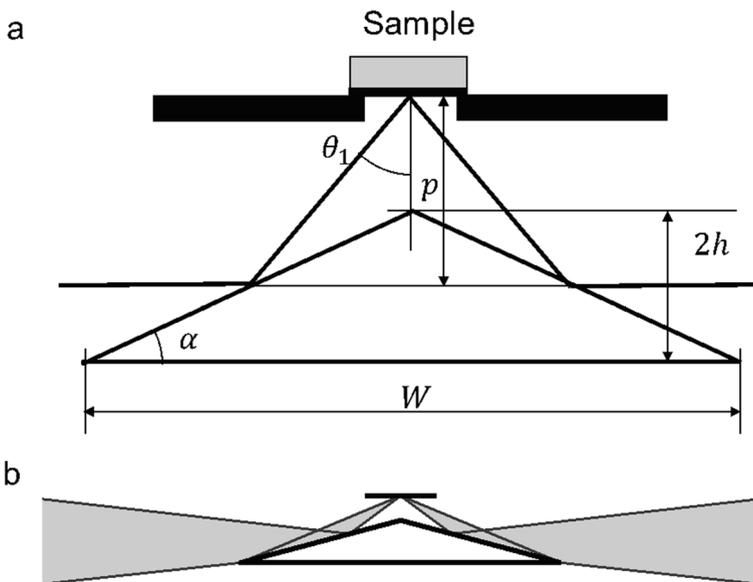
Fig. 4 **a** Design of the sample holder for THz spectroscopic ellipsometry. **b** The beam trajectory near the sample holder for $\theta_1 = 60°$. The cone angle of the beam probing the sample center corresponds to $NA = 0.125$

=0.6° in the case of $\theta_1 = 60°$ and the corresponding uncertainty of the surface conductivity for a thin film on a Si substrate is 0.05 mS.) owing to the long confocal length [2]. Therefore, $\Delta\theta_1$ is mainly determined by the misalignment of the sample holder. The accuracy of sample holder position can be increased by restricting the visible sample area with an aperture during the adjustment.

Note that, even for $\theta_1 = 60°$, the performance of this sample holder is greatly limited by the reflection condition at the mirror, where the incident angle is $90° - \alpha$ (=75° for $\theta_1 = 60°$). As θ_1 increases, the size of the holder increases and the incident angle at the mirror also increases, which distorts the polarization of the THz light. This can be seen from the fact that the dielectric constant of gold above 0.5 eV can be evaluated by ellipsometry using an angle of incidence of 75° [32]. To clarify the details, we calculated the polarization distortion of a THz pulse reflected from a gold surface (we calculated the Fresnel coefficients for s- and p-polarized light using the Drude parameters evaluated by spectroscopic ellipsometry above 0.5 eV). The refractive index of gold can be written as $n_2^2(\omega) = \epsilon_b - \omega_p^2/(\omega^2 + i\Gamma_p\omega)$, where $\epsilon_b = 1$, $\hbar\omega_p = 8.71$ eV, and $\hbar\,\Gamma_p = 0.048$ eV (ϵ_b is the background dielectric constant, ω_p is the plasma frequency, and Γ_p is the damping constant at room temperature).

The broken bold curves in Fig. 5 show the frequency dependence of $\rho = r_p/r_s$ for gold in the case of $\theta_1 = 75°$. At high frequencies, the reflection coefficient for p-polarized light is smaller than that for s-polarized light, and here the phase shift is also relatively large. On the other hand, at THz, the amplitude ratio is $\left|r_p/r_s\right| \approx 0.97$, and the phase difference is 27 mrad. Therefore, even for a gold mirror with an incident angle of 75°, it is necessary to compensate for polarization rotation. The polarization dependence of the gold mirror in the data can be removed by performing reference measurements where another gold mirror is placed at the sample position. As shown by the broken curve in Fig. 5, the deviation from $\left|r_p/r_s\right| \approx 1$ for $\theta_1 = 60°$ is about 40% of that for $\theta_1 = 75°$.

If the temperature dependence of ρ needs to be determined, we also need to consider that the temperature of the mirror changes during the measurement, and thus the polarization characteristics may change. In general, electron scattering in a metal increases with temperature. According to Ref. [32], the Drude parameters of gold at 470 K are $\epsilon_b = 1$, $\hbar\omega_p = 8.58$ eV, and $\hbar\,\Gamma_p = 0.067$ eV . Figure 5 shows that, in the case of $\theta_1 = 60°$ and a frequency of 1.8 THz, the difference between the phases at 470 K and 300 K is only 3 mrad. On the other hand, it is known that the morphology of a gold thin film can change at temperatures above 400 °C [32]. We also observed the formation of a copper–gold alloy at a temperature of 500 °C. Therefore, this sample holder should be operated in the temperature range below 400 °C.
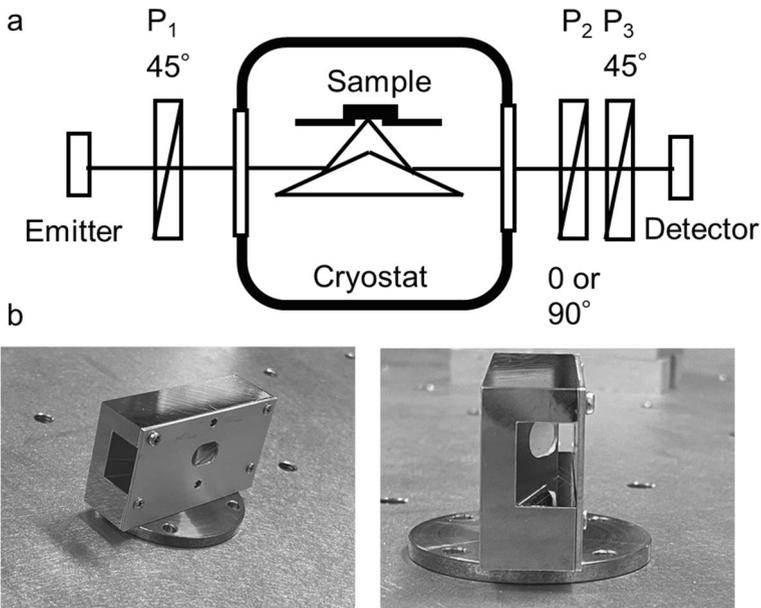
5 Experimental

In our experiment, an amplified Yb:KGW laser (Pharos, Light Conversion) with a repetition rate of 50 kHz, a pulse duration of 180 fs, and a pulse energy of 0.2 mJ was used as the light source. The output beam was split into one beam for THz pulse
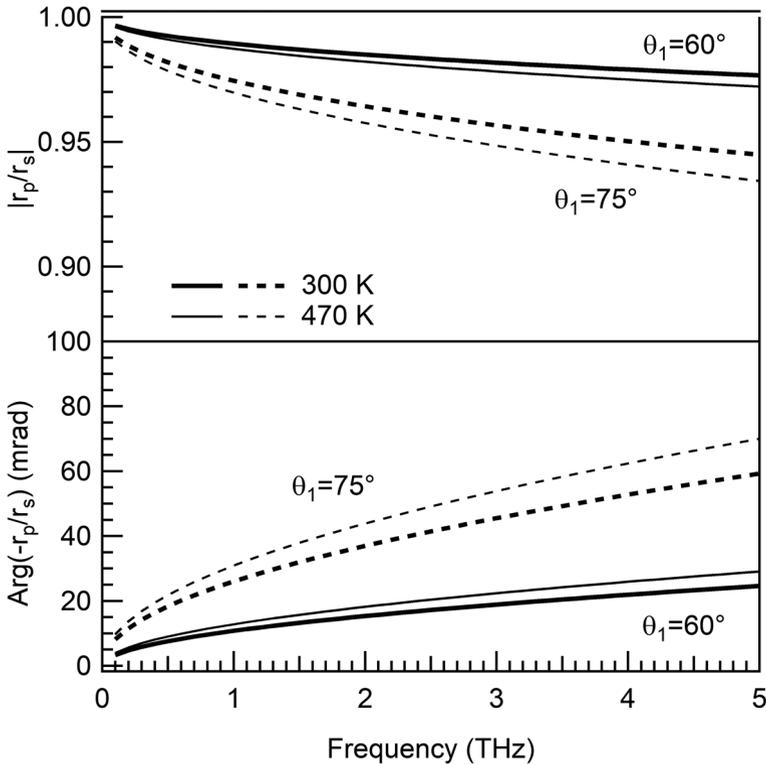
Fig. 5 Amplitude (upper panel) and phase (lower panel) of $\rho = r_p/r_s$ for gold at 300 K (bold curves) and 470 K (thin curves) in the case of $\theta_1 = 60°$ (solid curves) and $\theta_1 = 75°$ (broken curves)

generation and one beam for detection. The THz pulses generated in a 1-mm-thick (110) CdTe crystal [33] (Fig. 6a; emitter) were focused on the sample using two off-axis parabolic mirrors with effective focal lengths of 100 mm, and guided to the detector using further off-axis mirrors with effective focal lengths of 100 mm and 50 mm. We detected the THz electric field using a 1-mm-thick (110) CdTe crystal [33] (Fig. 6a; detector), and the polarization modulation induced by the THz electric field was digitized using a $\lambda/4$ plate, a Wollaston prism, and balanced detectors. We modulated the THz pulses at 0.8 kHz using an optical chopper to improve the signal-to-noise ratio. The signals from the balanced detectors at each sampling pulse delay time were digitized every 5,000 shots (corresponding to an accumulation time of 100 ms) using a data acquisition device (National Instruments, usb-6210), and the modulation components due to the THz electric field were extracted on a computer. The delay time of the sampling pulse was varied in 67 fs increments, obtaining a terahertz electric field time waveform with 256 data points. This electric field waveform does not include signals from back reflections on the InSb or substrates. As shown in Fig. 6a, we used three wire grid polarizers P_1, P_2, and P_3 for the THz spectroscopic ellipsometry measurements (these polarizers are the same as the one

Fig. 6 **a** Schematic of the experimental setup. (**b**) Photographs of the fabricated sample holder

described in Ref. [34]), and the effective diameter of the THz beam is mainly limited by their size (ø$=40$ mm). P_1 and P_3 were set to 45°, and P_2 was either set to 0° or 90°.

The fabricated sample holder with a prism for THz spectroscopic ellipsometry at $\theta_1 = 60°$ is shown in Fig. 6b. The prism was machined from a copper block, and then we polished the two mirror surfaces and used gold electroforming with a nickel layer. We attached the sample holder to a liquid N_2 cryostat (Cryo Industries of America, Inc.) with 3-mm-thick anhydrous silica windows. The thermal expansion of the cryostat may cause a vertical movement of the sample, but due to the chosen holder design this has only a small effect on the measurements. Before the experiment, we adjusted the THz spectroscopy system for operation in transmission geometry without our sample holder. Then, we inserted the cryostat, adjusted the position and azimuth of the sample holder to maximize the signal, and adjusted the positions of the CdTe crystals. For reference, we first performed THz spectroscopic ellipsometry measurements on a gold-plated copper plate in the temperature range 300–478 K. In this temperature range, we observed a phase drift of 15 mrad at 1.8 THz due to the temperature-dependent reflection coefficient of the gold mirrors and the gold reference plate. As expected from Fig. 5, the temperature-induced phase drift is negligible for our present purpose.

To verify the performance of this system, we performed THz spectroscopic ellipsometry measurements on undoped InSb in the temperature range 78–478 K. Figure 7a shows time-domain waveforms of the THz electric field reflected from the reference gold mirror and InSb. Since we also see a signal due to reflection at the rear surface, we calculated the Fourier transform of the data within a narrow time

range to determine the dielectric constant [2]. Figures 7b and 7c show the frequency dependence of the real part of the bulk dielectric constant ϵ of InSb and that of the real part of the bulk conductivity σ, respectively. We can confirm negative Re[ϵ] values at low frequencies and that Re[σ] increases with temperature. These are characteristics of the Drude response.

InSb has a small bandgap, and the density of thermally excited carriers increases with the temperature. We can further analyze the obtained THz dielectric constants using the Drude model, where we assumed a background dielectric constant of ϵ_b =16.8 [35]. The fitting results for the estimated plasma frequency and attenuation are shown in Fig. S4 of the Supplementary Information. We confirmed some deviations from the Drude model that are probably due to a phonon resonance, but here we would like to focus on the DC bulk conductivity σ. Figure 7d shows
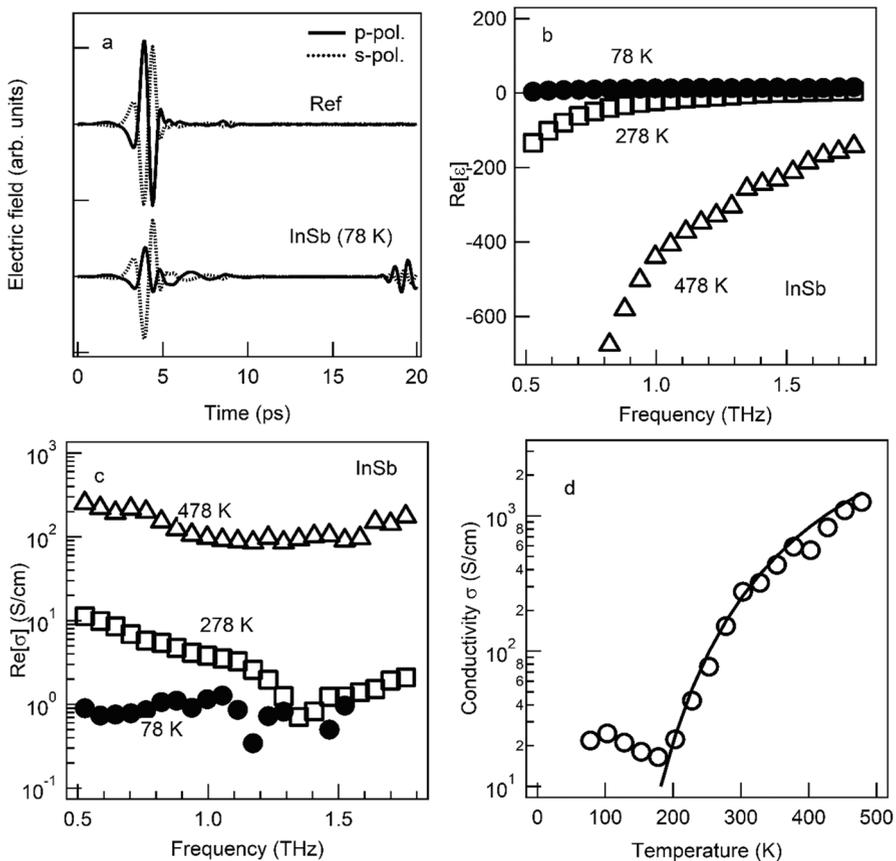
Fig. 7 **a** Time profiles of the reflected THz pulse for the reference sample and bulk undoped InSb. (**b**) The real part of ϵ and (**c**) the real part of σ of InSb at different temperatures. (**d**) The DC bulk conductivity evaluated by using our measurement method. The solid curve shows the empirical curve reported in Ref. [35]

the temperature dependence of σ of InSb; in the range above 180 K, σ gradually increases with the temperature. Previously reported DC conduction measurements of InSb have shown that the temperature dependence of the DC bulk conductivity of InSb can be described by $\sigma = e\mu N$, where $\mu = 1.09 \times 10^9 T^{-1.68}$ and $N^2 = 3.6 \times 10^{29} T^3 \exp(-0.26/k_B T)$ [36]. This theoretical temperature dependence is shown by the solid curve in Fig. 7d. Because our experimentally obtained σ roughly follows the same trend, we confirmed that our system can be used in the temperature range 78–478 K.

6 Evaluation of the Sheet Conductivities of Perovskite Rare-Earth Nickelate Thin Films

For the demonstration of the simplified characterization of thin films by THz time-domain spectroscopic ellipsometry, we focused on the rare-earth nickelates $NdNiO_3$ and $SmNiO_3$. These perovskites exhibit unique physical properties such as a metal–insulator transition due to strong electronic correlation, and it has been reported that the properties of rare-earth nickelates can be effectively modulated by chemical doping and proton doping [37]. By changing the ionic radius of the A-site cation, the tolerance factor can be changed, and the phase transition temperature can be tuned over a wide temperature range [38].

For this work, a $NdNiO_3$ thin film and a $SmNiO_3$ thin film were grown on $LaAlO_3$ substrates (10 mm × 10 mm) by pulsed laser deposition using an ArF excimer laser. The preparation technique can be found in Refs. [39–42]. The film thicknesses estimated using step measurements are 32 nm and 15 nm for the $NdNiO_3$ and $SmNiO_3$ thin films, respectively, and for the initial characterization, we performed X-ray diffraction measurements and DC resistance measurements (the results are shown in Figs. S5 and S6 of the Supplementary Information).

In spite of being a popular substrate for perovskite oxide thin films, $LaAlO_3$ exhibits dielectric dispersion [43], absorption, birefringence [44], and twinning, which make conventional THz transmission spectroscopy for thin film samples difficult, because here the interaction length in the substrate is much longer than that in the film. The uncertainty in the refractive index is $\Delta n_2 \approx 0.1$, and the corresponding uncertainty of the sheet conductivity in spectroscopic ellipsometry is $\Delta\sigma_s \approx \Delta n_2 / Z_0 = 0.3$ mS according to Eq. (5). For the analysis, we used $n_2 = 5.0$.

Figures 8a and 8b show the real parts of sheet conductivity of the $NdNiO_3$ and $SmNiO_3$ thin films, respectively, evaluated by THz time-domain spectroscopic ellipsometry for two characteristic temperatures: above and below the so-called critical temperature T_c. The sheet conductivities are low below T_c and high above T_c. Their imaginary parts of sheet conductivity are shown in Fig. S7 of the Supplementary Information. The data points in Figs. 8c and 8d show the corresponding temperature dependences of the average sheet conductivity in the range of frequencies from 0.9 THz to 1.1 THz. The electric sheet conductivity measured while increasing the temperature is shown by the solid curves. We find that the electric sheet conductivity is approximately the same as the THz sheet conductivity.
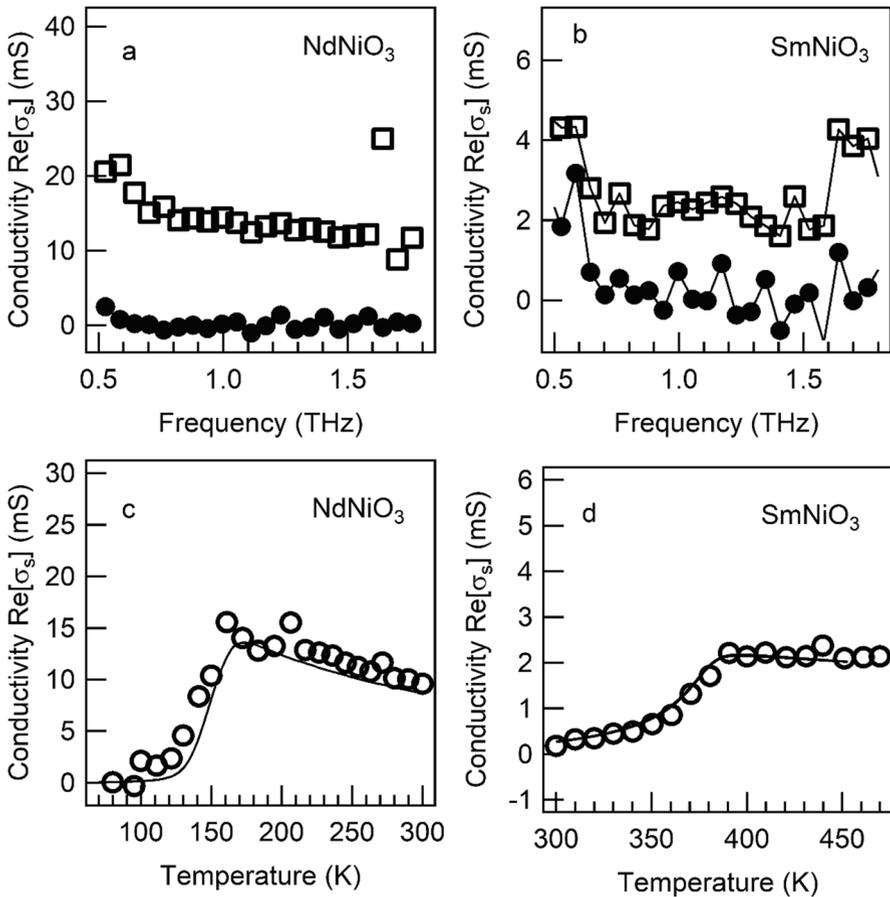
Fig. 8 Real parts of sheet conductivity for (**a**) the $NdNiO_3$ and (**b**) the $SmNiO_3$ thin films evaluated by THz time-domain spectroscopic ellipsometry. The temperature dependence of the average sheet conductivity in the range of frequencies from 0.9 THz to 1.1 THz for $NdNiO_3$ and $SmNiO_3$ is shown in (**c**) and (**d**), respectively. The solid curves show the sheet conductivities determined from electrical measurements (the data was taken while the temperature was increased)

7 Conclusion

We have presented two ideas to simplify the characterization of ultrathin conductive films by THz time-domain spectroscopic ellipsometry. We proposed to use an analytical model for the evaluation of the recorded data, in which the thin film is treated as a single interface with a certain sheet conductivity σ_s. This model is valid for thin film thicknesses much smaller than the used wavelength ($d < 1$ μm). For the actual experiments, we presented a sample-holder design of the cryostat that enables us to perform THz spectroscopic ellipsometry measurements of thin films by inserting the holder into a conventional THz spectroscopy system for measurements in transmission geometry. We evaluated the sheet conductivities

of rare-earth nickelate thin films in the temperature range 78–478 K. The demonstrated approach is a powerful method for the evaluation of semiconductor thin films, two-dimensional materials such as graphene, and topological insulators. The presented ideas will help many researchers concerned with the measurement and analysis of THz spectroscopy ellipsometry data of ultrathin conductive films to save time.

Data Availability All data necessary to evaluate the paper's conclusions are provided in the paper and/or its supporting information. All other data are available from the corresponding author on reasonable request.

Declarations

Competing Interests The authors declare no competing interests.

References

1. H. Fujiwara, "Spectroscopic Ellipsometry: Principles and Applications" (John Wiley& Sons, 2007).
2. X. Chen and E. Pickwell-MacPherson, "An introduction to terahertz time-domain spectroscopic ellipsometry," *APL Photon.* vol. **7**, 071101 Jul. 2022, https://doi.org/10.1063/5.0094056.
3. B. Ferguson and X.C. Zhang," Materials for terahertz science and technology," *Nat. Mat.* vol. **1**, pp. 26–33 Sep. 2002. https://doi.org/10.1038/nmat708.
4. J. F. O'Hara, W. Withayachumnankul, and I. Al-Naib, "A Review on Thin-film Sensing with Terahertz Waves," *J. Infrared Milli Terahz Waves* vol. **33**, pp. 245–291 Mar. 2012, https://doi.org/10.1007/s10762-012-9878-x.

5. S. Nashima, O. Morikawa, K. Takata, and M. Hangyo, "Measurement of optical properties of highly doped silicon by terahertz time domain reflection spectroscopy," *Appl. Phys. Lett.* vol. **79**, pp. 3923-3925, Dec. 2001, https://doi.org/10.1063/1.1413498.

6. A. Pashkin, M. Kempa, H. Němec, F. Kadlec, and P. Kužel, "Phase-sensitive time-domain terahertz reflection spectroscopy," *Rev. Sci. Instrum.* vol. **74**, pp. 4711–4717 Nov, 2003, https://doi.org/10.1063/1.1614878.

7. T. Nagashima; M. Hangyo, "Measurement of complex optical constants of a highly doped Si wafer using terahertz ellipsometry," *Appl. Phys. Lett.* vol. **79**, pp. 3917–3919 Dec. 2001, https://doi.org/10.1063/1.1426258.

8. M. Schubert, T. Hofmann, and C. M. Herzinger, "Generalized far-infrared magneto-optic ellipsometry for semiconductor layer structures: determination of free-carrier effective-mass, mobility, and concentration parameters in n-type GaAs," *J. Opt. Soc. Am A* vol. 20 pp. 347-56 Feb. 2003, https://doi.org/10.1364/josaa.20.000347.

9. C. Bernhard, J. Humlícek, and B. Keimer, "Far-infrared ellipsometry using a synchrotron light source—the dielectric response of the cuprate high T$_c$ superconductors," *Thin Solid Films* vol. **455–456**, pp. 143–149, May 2004, https://doi.org/10.1016/j.tsf.2004.01.002

10. T. Hofmann, U. Schade, C. M. Herzinger, P. Esquinazi, and M. Schubert, "Terahertz magneto-optic generalized ellipsometry using synchrotron and blackbody radiation," *Rev. Sci. Instrum.* vol. **77**, 063902 Jun. 2006, https://doi.org/10.1063/1.2209968.

11. T. Hofmann, C. M. Herzinger, A. Boosalis, T. E. Tiwald, J. A. Woollam, and M. Schubert, "Variable-wavelength frequency-domain terahertz ellipsometry," *Rev. Sci. Instrum.* vol. **81**, 023101 Feb. 2010, https://doi.org/10.1063/1.3297902.

12. N. Matsumoto, T. Hosokura, T. Nagashima, and M. Hangyo, "Measurement of the dielectric constant of thin films by terahertz time-domain spectroscopic ellipsometry," *Opt. Lett.* vol. **36**, pp. 265-267 Jan. 2011, https://doi.org/10.1364/OL.36.000265.

13. M. Neshat and N. P. Armitage, "Terahertz time-domain spectroscopic ellipsometry: instrumentation and calibration," *Opt. Express*, vol. **20**, pp. 29063-29075 Jan. 2012, https://doi.org/10.1364/OL.36.000265.

14. P. Marsik, K. Sen, J. Khmaladze, M. Yazdi-Rizi, B. P. P. Mallett, C. Bernhard, "Terahertz ellipsometry study of the soft mode behavior in ultrathin SrTiO$_3$ films," *Appl. Phys. Lett.* vol. **108**, 052901 Feb. 2016, https://doi.org/10.1063/1.4940976.

15. P. Kühne, N. Armakavicius, V. Stanishev, C. M. Herzinger, M. Schubert and V. Darakchieva, "Advanced Terahertz Frequency-Domain Ellipsometry Instrumentation for In Situ and Ex Situ Applications," *IEEE Trans. Terahertz Sci. Technol.* vol. 8, no. 3, pp. 257-270, Apr. 2018, https://doi.org/10.1109/TTHZ.2018.2814347.

16. P. Gopalan, S. Knight, A. Chanana, M. Stokey, P. Ranga, M. A. Scarpulla, S. Krishnamoorthy, V. Darakchieva, Z. Galazka, K. Irmscher, A. Fiedler, S. Blair, M. Schubert, and B. Sensale-Rodriguez, "The anisotropic quasi-static permittivity of single-crystal β-Ga$_2$O$_3$ measured by terahertz spectroscopy," *Appl. Phys. Lett.* vol. **117**, 252103 Dec. 2020, https://doi.org/10.1063/5.0031464.

17. S. Knight, S. Schöche, P. Kühne, T. Hofmann, V. Darakchieva, and M. Schubert, "Tunable cavity-enhanced terahertz frequency-domain optical Hall effect," *Rev. Sci. Instrum.* vol. **91**, 083903 Aug. 2020, https://doi.org/10.1063/5.0010267.

18. A. Belyaeva, Alexey Galuza, I. Kolenov, and S. Mizrakhy, "Developments in Terahertz Ellipsometry: Portable Spectroscopic Quasi-Optical Ellipsometer-Reflectometer and Its Applications", *J. Infrared Milli. Terahz Waves* vol. **42**, pp. 130–153 Jan. 2021, https://doi.org/10.1007/s10762-020-00762-7.

19. V. C. Agulto, T. Iwamoto, H. Kitahara, K. Toya, V. K. Mag-usara, M. Imanishi, Y. Mori, M. Yoshimura and M. Nakajima, "Terahertz time-domain ellipsometry with high precision for the evaluation of GaN crystals with carrier densities up to 10^{20} cm^{-3}," *Sci. Rep.* vol. **11**, 18129 Sep. 2021, https://doi.org/10.1038/s41598-021-97253-z.

20. H. Ketelsen, R. Mästle, L. Liebermeister, R. Kohlhaas, and B. Globisch, "THz Time-Domain Ellipsometer for Material Characterization and Paint Quality Control with More Than 5 THz Bandwidth," *Appl. Sci.* vol. **12**, 3744 Apr. 2022, https://doi.org/10.3390/app12083744.

21. Z. Mazaheri, C. Koral, and A. Andreone, "Accurate THz ellipsometry using calibration in time domain," *Sci. Rep.* vol. **12**, 7342, May 2022, https://doi.org/10.1038/s41598-022-10804-w.

22. H. Lin, P. Braeuninger-Weimer, V. S. Kamboj, D.S. Jessop, R. Degl'Innocenti, H. E. Beere, D. A. Ritchie, J. A. Zeitler and S. Hofmann, "Contactless graphene conductivity mapping on a wide range

of substrates with terahertz time-domain reflection spectroscopy," *Sci. Rep.* vol. **7**, 10625, Sep. 2017, https://doi.org/10.1038/s41598-017-09809-7.

23. L. Ding, T. Qiu, J. Zhang and X. Wen, "Generalized Brewster effect tuned optically in a graphene/substrate system," *J. Opt.* vol. **21**, 125602, Nov. 2019, https://doi.org/10.1088/2040-8986/ab4fa1.

24. M. Tinkham, "Energy Gap Interpretation of Experiments on Infrared Transmission through Superconducting Films," *Phys. Rev.* vol. 104, pp. 845-846 Nov. 1956, https://doi.org/10.1103/PhysRev.104.845.

25. H. Hirori, K. Yamashita, M. Nagai, and K. Tanaka, "Attenuated total reflection spectroscopy in a time domain using terahertz coherent pulses," *Jpn. J. Appl. Phys.* vol. **43**, pp. L1287-L1289 Sep. 2004, https://doi.org/10.1143/JJAP.43.L1287.

26. M. Nagai, H. Yada, T. Arikawa, and K. Tanaka, "Terahertz time-domain attenuated total reflection spectroscopy in water and biological solution," *Int. J. Infrared and Millimeter Waves*, vol. **27**, 505-515 Feb. 2006, https://doi.org/10.1007/s10762-006-9098-3.

27. G. Yamashita, E. Matsubara, M. Nagai, Y. Kanemitsu and M. Ashida, "Intrinsic carrier multiplication efficiency in bulk Si crystals evaluated by optical-pump/terahertz-probe spectroscopy," *Appl. Phys. Lett.* vol. **105**, 231118 (2014).

28. G. Yamashita, E. Matsubara, M. Nagai, C. Kim, H. Akiyama, Y. Kanemitsu, and M. Ashida, "Sensitive monitoring of photocarrier densities in the active layer of a photovoltaic device with time-resolved terahertz reflection spectroscopy," *Appl. Phys. Lett.* vol. **110**, 071108 Dec. 2017, https://doi.org/10.1063/1.4903859.

29. M. Nagai, T. Tomioka, M. Ashida, M. Hoyano, R. Akashi, T. Yamada, T. Aharen, and Y. Kanemitsu, "Longitudinal Optical Phonons Modified by Organic Molecular Cation Motions in Organic-Inorganic Hybrid Perovskites," *Phys. Rev. Lett.* vol. 121, 145506 Oct. 2018, https://doi.org/10.1103/PhysRevLett.121.145506.

30. H. Watanabe, D. Wang, T. Fujii, T. Iwamoto, T. Fukuda, M. Deura, and Tsutomu Araki, "Investigation of non-destructive and non-contact electrical characterization of $< 1\mu m$ thick GaN thin films on $ScAlMgO_4$ substrates by THz-TDSE," *Phys. Status Solidi* B 2400017 Apr. 2024, https://doi.org/10.1002/pssb.202400017.

31. M. Li, J. Fortin, J Y. Kim, G. Fox, F. Chu, T. Davenport, Toh-Ming Lu, and X-C Zhang, "Dielectric Constant Measurement of Thin Films Using Goniometric Terahertz Time-Domain Spectroscopy," *IEEE J. Sel. Top. Quantum Electron.* vol. 7, no. 4, pp. 624–629, July-Sept. 2001, https://doi.org/10.1109/2944.974234.

32. H. Reddy, U. Guler, A. V. Kildishev, A. Boltasseva, and V. M. Shalaev, "Temperature-dependent optical properties of gold thin film*s*," *Opt. Mat. Express* vol. **6**, no. 9 pp. 2776-2802 Aug. 2016, https://doi.org/10.1364/OME.6.002776

33. A. Syouji, S. Saito, K. Sakai, M. Nagai, K. Tanaka, H. Ohtake, T. Bessho, T. Sugiura, T. Hirosumi, and M. Yoshida, "Evaluation of a terahertz wave spectrum and construction of a terahertz wave-sensing system using a Yb-doped fiber laser," *J. Opt.l Soc. Am.* B, vol. 24, pp. 2006–2012, Jul. 2007, https://doi.org/10.1364/JOSAB.24.002006.

34. K. Miyagawa, M. Nagai, M. Ashida, C. Kim and H. Akiyama, "Enhanced Magneto-Optical Kerr Effect of GaAs-Based P-N Junctions in the Terahertz Range," *J Infrared Milli Terahz Waves* vol. **42**, pp. 325–337 Feb. 2021, https://doi.org/10.1007/s10762-021-00779-6.

35. J.R. Dixon, and J.K. Furdyna, "Measurement of the static dielectric constant of the InSb lattice via gyrotropic sphere resonances," *Solid state Commun.* vol. 35, pp. 195-198 Jul. 1980, https://doi.org/10.1016/0038-1098(80)90244-6.

36. H. J. Hrostowski, F. J. Morin, T. H. Geballe, and G. H. Wheatley, "Hall Effect and Conductivity of InSb," *Phys. Rev.* vol. **100**, pp. 1672-1676 Dec. 1955, https://doi.org/10.1103/PhysRev.100.1672.

37. M. L. Medarde, "Structural, magnetic and electronic properties of $RNiO_3$ perovskites (R = rare earth)," *J. Phys.: Condens. Matter* vol. **9** 1679–1707, 1997, https://doi.org/10.1088/0953-8984/9/8/003.

38. J. B. Torrance, P. Lacorre, A. I. Nazzal, E. J. Ansaldo, and Ch. Niedermayer, "Systematic study of insulator-metal transitions in perovskites $RNiO_3$ (R=Pr,Nd,Sm,Eu) due to closing of charge-transfer gap," *Phys. Rev. B* vol. **45**, pp. 8209R-8212R Apr. 1992, https://doi.org/10.1103/PhysRevB.45.8209.

39. H. Ren, A. I. Osaka, A. N. Hattori, B. Yu, M. Nagai, M. Ashida, B. Li, C. Zou, and Hidekazu Tanaka, "Controllable Strongly Electron-Correlated Properties of $NdNiO_3$ Induced by Large-Area Protonation with Metal–Acid Treatment," *ACS Appl. Electron. Mater.*, vol. **4**, pp. 3495–3502 Jun. 2022, https://doi.org/10.1021/acsaelm.2c00473.

40. U. Sidik, A. N. Hattori, A. N. Hattori, K. Hattori, M. Alaydrus, I. Hamada, L. N. Pamasi, and H. Tanaka, "Tunable Proton Diffusion in NdNiO$_3$ Thin Films under Regulated Lattice Strains," *ACS Appl. Electron. Mater.* vol. **4,** pp. 4849–4856 Oct. 2022, https://doi.org/10.1021/acsaelm.2c00711.

41. Y. Taniguchi, H.-B. Li, A. N. Hattori, and H. Tanaka, Comprehensive determination of proton diffusion in protonated NdNiO$_3$ thin film by a combination of electrochemical impedance spectroscopy and optical observation, *Appl. Phys. Express* vol. **16**, 035501 Mar. 2023, https://doi.org/10.35848/1882-0786/acc004.

42. Y. Taniguchi, H.-B. Li, K. Shimoyama, A. N. Hattori, H. Tanaka, "Epitaxial growth of EuNiO$_3$ on SrTiO$_3$ and its application to stacked protonation resistance switching devices," *Appl. Phys. Lett.* vol. **122**, 263502 Jun. 2023, https://doi.org/10.1063/5.0152640.

43. D. Grischkowsky and S. Keiding, "THz time-domain spectroscopy of high Tc substrates," *Appl. Phys. Lett.* vol. **57**, pp. 1055-1057 Sep. 1990, https://doi.org/10.1063/1.104280.

44. J. Lloyd-Hughes, S. P. P. Jones, E. Castro-Camus, K. I. Doig, and J. L. MacManus-Driscoll, "Modifying the polarization state of terahertz radiation using anisotropic twin-domains in LaAlO$_3$," *Opt. Lett.* vol. **39**, pp. 1121-1124 Feb. 2014, https://doi.org/10.1364/OL.39.001121.